Measurements and Computations of Second-Mode Instability Waves in Three Hypersonic Wind Tunnels

Dennis C. Berridge[*]

School of Aeronautics and Astronautics, Purdue University, West Lafayette, IN 47907-1282

Katya M. Casper[†]

School of Aeronautics and Astronautics, Purdue University, West Lafayette, IN 47907-1282

Sandia National Laboratories, Albuquerque, NM 87185

Shann J. Rufer[‡]

NASA Langley Research Center, Hampton, VA 23681

Christopher R. Alba[§]

Air Vehicles Directorate, Air Force Research Laboratory, Wright-Patterson AFB, OH 45433

Daniel R. Lewis[¶]

Aerospace Testing Alliance, Silver Spring, MD 20903-1005

Steven J. Beresh[‖]

Sandia National Laboratories, Albuquerque, NM 87185

Steven P. Schneider[**]

School of Aeronautics and Astronautics, Purdue University, West Lafayette, IN 47907-1282

High-frequency pressure-fluctuation measurements were made in AEDC Tunnel 9 at Mach 10 and the NASA Langley 15-Inch Mach 6 and 31-Inch Mach 10 tunnels. Measurements were made on a $7°$-half-angle cone model. Pitot measurements of freestream pressure fluctuations were also made in Tunnel 9 and the Langley Mach-6 tunnel. For the first time, second-mode waves were measured in all of these tunnels, using 1-MHz-response pressure sensors. In Tunnel 9, second-mode waves could be seen in power spectra computed from records as short as 80 μs. The second-mode wave amplitudes were observed to saturate and then begin to decrease in the Langley tunnels, indicating wave breakdown. Breakdown was estimated to occur near $N \approx 5$ in the Langley Mach-10 tunnel. The unit-Reynolds-number variations in the data from Tunnel 9 were too large to see the same processes. In Tunnel 9, the measured transition locations were found to be at $N = 4.5$ using thermocouples, and

[*]Research Assistant, Student Member, AIAA

[†]Graduate Research Assistant and Student Intern, Student Member, AIAA

[‡]Aerospace Engineer, Aerothermodynamics Branch, Member, AIAA

[§]1Lt, USAF, Member, AIAA

[¶]Project Engineer, Senior Member, AIAA

[‖]Principal Member of the Technical Staff, Engineering Sciences Center, Associate Fellow AIAA

[**]Professor, Associate Fellow, AIAA

American Institute of Aeronautics and Astronautics

$N = 5.3$ using 50-kHz-response pressure sensors. What appears to be a very long transitional region was observed at a unit Reynolds number of 13.5 million per meter in Tunnel 9. These results were consistent with the high-frequency pressure fluctuation measurements. High-frequency pressure fluctuation measurements indicated that transition did occur in the Langley Mach-6 tunnel, but the location of transition was not precisely determined. Unit Reynolds numbers in the Langley Mach-10 tunnel were too low to observe transition. More analysis of this data set is expected in the future.

Nomenclature

A	disturbance amplitude		
A_0	initial disturbance amplitude		
D	diameter (m)	*Subscript*	
f	frequency (kHz)	0	stagnation condition
M	Mach number	*mean*	average (mean)
N	integrated amplification factor	w	wall condition
P, p	pressure (kPa)	θ	momentum thickness
Re	Reynolds number		
St	Stanton number	*Abbreviations*	
T	temperature (K)	AEDC	Arnold Engineering Development Center
t	time (seconds)	DPLR	Data-Parallel Line Relaxation
x	cone axial coordinate (m)	LaRC	NASA Langley Research Center
ϕ	cone azimuthal coordinate (degrees)	LST	Linear Stability Theory
		PSD	Power Spectral Density
Superscript		PSE	Parabolized Stability Equations
$'$	fluctuations	RMS	Root Mean Square

I. Introduction

Linear stability theory predicts that second-mode disturbances will be most unstable when there exists in the boundary layer a region of supersonic flow relative to the disturbance phase velocity. Calculations have shown that the second-mode instability is dominant, compared to the first-mode instability, when the edge Mach number is sufficiently high for a given wall temperature ($M \gtrsim 5$). First identified by Mack, second-mode instabilities are characterized as high frequency, acoustic wave disturbances.[1] Stetson *et al.*[2] and Stetson and Kimmel[3] have used hot-wire anemometry to measure second-mode instabilities in a conventional wind tunnel. Similar measurements have been carried out in both noisy and quiet flow.[4] These measurements are very difficult due to the limited mechanical strength of small hot wires with sufficiently high frequency response. In addition, since hot wires are intrusive, measurements can only be taken at a single streamwise position at any one time, requiring multiple runs at the same condition. These two disadvantages combine to make instability measurements with hot wires impossible or prohibitively expensive in many hypersonic tunnels. Because of this, robust and non-intrusive alternatives are desirable. Recently, Fujii[5] has shown that fast surface pressure sensors can detect second-mode waves on a cone in noisy hypersonic flow. Other measurements have since been made with these sensors in multiple tunnels under noisy and quiet flow.[6–9] These sensors show promise for being able to measure boundary-layer instabilities in many hypersonic wind tunnels.

Measurements of boundary-layer instabilities in hypersonic tunnels are needed in order to improve methods for predicting transition in flight using theory, computation and ground tests. Simple empirical correlations, such as Re_θ/M_e (Reynolds number based on momentum thickness divided by the edge Mach number) do not account for the mechanisms of transition, making it difficult to extrapolate results from each partial ground simulation to flight. Semi-empirical methods, such as e^N, use the growth of instabilities to predict transition location. Instability growth is computed as a ratio, $A/A_0 = e^N$, where A is the amplitude at a given location, and A_0 is the amplitude at the location at which the instability first starts to amplify. Transition is then empirically correlated to a certain N factor. However, much is still uncertain when using e^N to predict transition. The initial amplitude of the instabilities is not accounted for, nor is it known at what amplitude the instabilities will break down.

American Institute of Aeronautics and Astronautics

Tunnel noise has been shown to have an impact on transition location, as well as the N factors at which transition occurs.[10] In flight, as well as in quiet tunnels, transition seems to occur at N factors between 8 and 11.[11,12] Exceptions to this have been found, as in Reference 13. In conventional tunnels, transition usually occurs at N factors around 5.[14] Pate also showed that transition on sharp cones at zero angle of attack can be correlated to measurements of tunnel noise.[15] While quiet tunnels can more accurately simulate flight noise levels, they are incapable of high Reynolds numbers, high Mach numbers, and high enthalpy. Since no single tunnel is able to simulate all aspects of flight, transition measurements must be made in multiple wind tunnels. If the effect of tunnel noise on transition can be understood, and measurements of boundary-layer instabilities can be made in the tunnels in which vehicles undergo testing, methods for extrapolating transition location from ground test to flight can further incorporate the physics of transition, improving accuracy and reducing risk. This is particularly critical since hypersonic flight tests are about a hundred times more expensive than ground tests, and generally return less data.

The present measurements were made as part of an effort to show that boundary-layer instabilities can be measured in large conventional hypersonic tunnels, and to better determine the effect of tunnel noise on transition. Pressure fluctuation and heat transfer measurements were made on a 7° half-angle cone to locate transition and measure boundary-layer instabilities, and compared to computations of instability growth. Pitot probe measurements of freestream noise were also made to compare to the pressure fluctuations measured in the model boundary layer. The growth of the instabilities was also computed using the University of Minnesota's STABL software suite.

II.   Experimental Setups

A.   AEDC Tunnel 9 Facility

Tunnel 9 is a unique blowdown facility that uses pure nitrogen as the working fluid and currently operates at Mach numbers 7, 8, 10 and 14. All tests for this work were performed at Mach 10. An operational envelope showing Reynolds number equivalent altitudes versus Mach number for Tunnel 9 operating conditions is presented in Figure 1. The unit Reynolds number range for the facility is from 0.16×10^6/m (useful for high-altitude/viscous interaction simulation) to 158×10^6/m (duplication of flight dynamic pressure). Usable test periods in Tunnel 9 range from 0.25 s to over 15 s, depending on test conditions. The test section is over 3.6 m long and has a diameter of 1.5 m, enabling testing of large-scale model configurations that can include simultaneous force and moment, pressure, and heat-transfer instrumentation. The Mach 10 and 14 nozzles are 12.2 m in length with a 1.5-m-diameter exit. A schematic of the entire facility is shown in Figure 2.
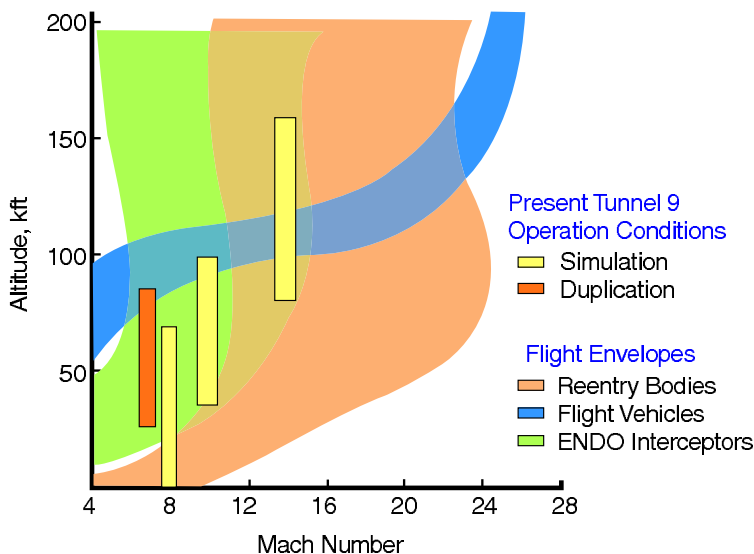

Figure 1: Hypervelocity Wind Tunnel 9 operational envelope.

During a typical run, the vertical heater vessel is used to pressurize and heat a fixed volume of nitrogen to a predetermined pressure and temperature. The test cell and vacuum sphere are evacuated to approximately
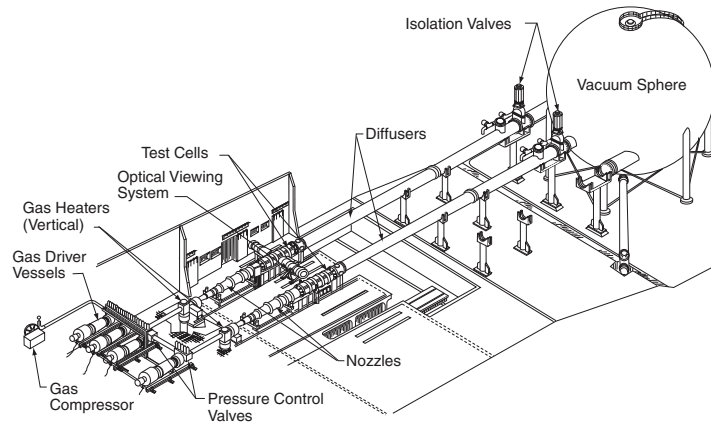
Figure 2: Hypervelocity Wind Tunnel 9 facility schematic.

1 mm Hg and are separated from the heater by a pair of metal diaphragms. When the desired temperature and pressure are reached in the heater, the diaphragms are ruptured. The gas then flows from the top of the heater vessel, expanding through the contoured nozzle into the test section at the desired free-stream test conditions. As the hot gas exhausts from the top of the heater, cooler nitrogen gas from the pressurized driver vessels enters the heater base. This cold gas drives the hot gas out the top of the heater in a piston-like fashion, thereby maintaining constant conditions in the nozzle supply plenum and the test section during the run. A more complete description of the Tunnel 9 facility and its capabilities can be found in Reference 16.

Multiple models were installed in the tunnel during these tests, which required the cone used for these measurements to be mounted 0.3058 m off the center axis of the test section. The test cell is shown in Figure 3. The cone is in the lower right, with a waverider model installed in the center of the tunnel. The pitot probes are at the top of the test section, and a hemisphere model is visible in the lower left. The cone is mounted so that the pressure sensors face upwards. Both rows of sensors are 60° off the vertical, with one row pointing towards the wall and the other pointing towards the center of the tunnel. This may have affected the noise environment around the cone. The Pitot probes were also off-center by 0.419 m.

B.   NASA Langley Tunnels

1.   31-Inch Mach 10 Tunnel

The NASA Langley 31-Inch Mach-10 Air Tunnel[17] is a blow-down wind tunnel that uses dry air as the test gas. The unit Reynolds number range for the tunnel is $Re/m = 1.6 \times 10^6$ to $Re/m = 6.9 \times 10^6$. The facility consists of a high pressure air storage system having a volume of 24.5 m^3 and rated at 30.3×10^4 kPa maximum, a 12.5-MW electrical resistance heater located in a vertical pressure vessel, a 5-micron in-line filter, settling chamber, three dimensional contoured nozzle, 0.787-m square closed test section with a 0.36 m inviscid core., adjustable second minimum, after cooler, steam ejector, vacuum spheres and vacuum pumps. The settling chamber, nozzle throat section, test section, adjustable second minimum, and subsonic diffuser are all water cooled. The 0.304-m diameter settling chamber is equipped with screens at the upstream end and is faired into the upstream end of a square cross section nozzle having a 2.72-cm square throat. The throat section is one piece fabricated from beryllium copper, and backside water-cooled with the cooling water system operating at 3450 kPa. Models are supported on a hydraulically-operated, sidewall-mounted injection system. The angle of attack can be varied from −90° to +90°, and the sideslip range is ±5°.

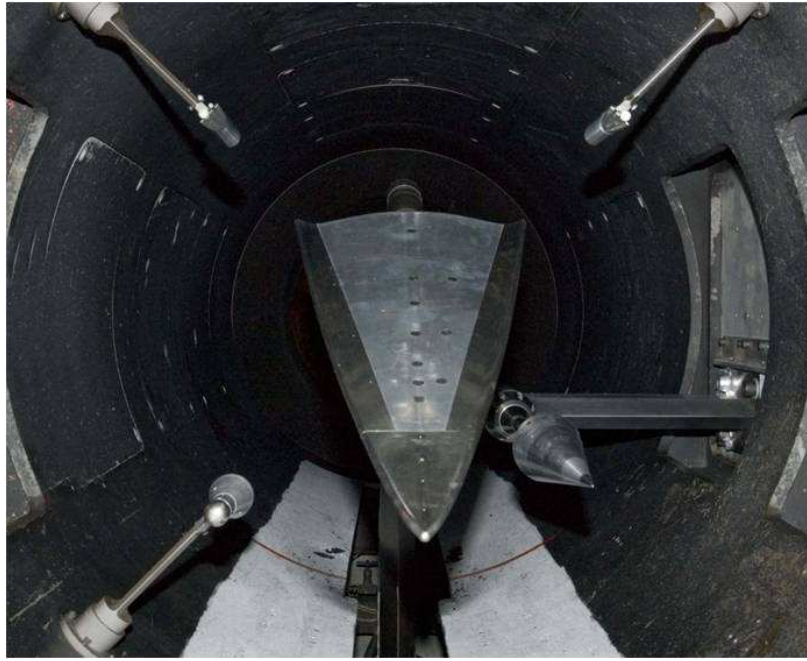American Institute of Aeronautics and Astronautics

Figure 3: View of the Tunnel 9 test section as set up during these tests.

With the second minimum closed to about 25% of the maximum test section cross section area and the use of two 12.5-m diameter vacuum spheres, run times up to two minutes can be achieved. However, heating tests generally only have total run times of 30 seconds, with actual model residence time on tunnel centerline of approximately 5-10 seconds.

2. 15-Inch Mach 6 Hi-Temperature Tunnel

The basic components of the NASA Langley 15-Inch Mach 6 Hi-Temperature Tunnel include an 24.5 m^3 bottle field; a 5–MW AC resistance heater mounted vertically to accommodate thermal expansion which consists of 216 electrically-heated tubes through which the air flows; 5 micron in-line filter; pressure regulator; settling chamber; an axisymmetric contoured nozzle having a throat diameter of 4.60 cm; nozzle exit diameter of 0.37 m; a length of 1.92 m; a walk-in open-jet test section with numerous accesses; a hydraulically-driven injection/retraction support mechanism for which the angle of attack may be varied from -10° to 50° and sideslip between ±10°; variable area diffuser; an aftercooler; and a vacuum system shared with the 31-Inch Mach 10 Tunnel. The electrical heater is capable of heating the air to 833 K at a maximum pressure of 3450 kPa. The tunnel is capable of running conditions between $Re/m = 4.9 \times 10^6$ and $Re/m = 24.3 \times 10^6$.

C. Model and Instrumentation

The model used in these tests is a 0.517-m-long 7° half-angle stainless-steel cone. A sharp nose tip (radius less than 0.05 mm) was used for the majority of these tests. There are two rows for instrumentation spaced 120° apart, with a third row installed 300° counter-clockwise from the first row, looking from the rear of the cone. Two of the rows have inserts which allow the installation of multiple types of sensors. The third row consists of 12 surface-mounted Medtherm Type-E coaxial thermocouples spaced 0.025 m apart, beginning at $x = 0.222$ m and ending at $x = 0.522$ m. This third row was added after the tests at NASA Langley took place, so these sensors were only available at Tunnel 9. The locations of the three rows are shown in Figure 4 and Table 1 lists the location of these sensors, where x is the axial distance from the sharp nose tip and ϕ is the cone azimuthal angle. Two Dantec type 55R47 hot-films were also installed on the cone at $x = 0.452$ m and $x = 0.490$ m. More details about the cone, instrumentation and experiments are given in Reference 18.

The growth and breakdown of the second-mode wave instability was studied with PCB132 sensors. The PCB132s were used to measure pressure fluctuations between 11 kHz and 1 MHz. The resonant frequency of
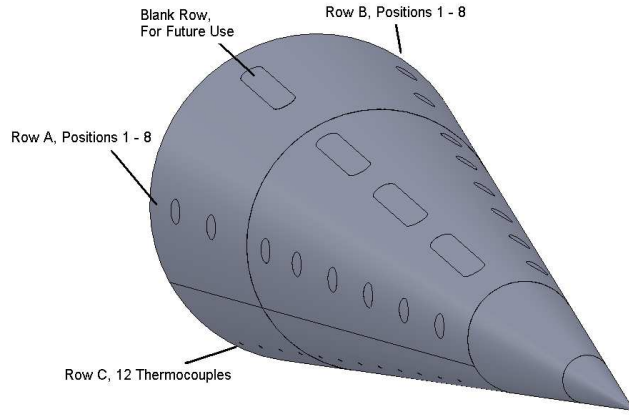
Figure 4: Diagram of cone showing sensor insert locations

Location	x (m)	ϕ (degrees)	Sensor Type	Location	x (m)	ϕ (degrees)	Sensor Type
1A	0.208	0	PCB132	1B	0.208	120	PCB132
2A	0.246	0	Kulite	2B	0.246	120	Kulite
3A	0.284	0	Kulite	3B	0.284	120	Thermocouple
4A	0.322	0	Kulite	4B	0.322	120	Kulite
5A	0.360	0	PCB132	5B	0.360	120	PCB132
6A	0.398	0	Kulite	6B	0.398	120	Kulite
7A	0.452	0	Kulite	7B	0.452	120	Microphone
8A	0.490	0	PCB132	8B	0.490	120	PCB 132

Table 1: Individual sensor locations for the two sensor insert rows.

the sensor is above 1 MHz and the sensor output is high-pass filtered with a 3-dB cutoff frequency at 11 kHz. Because of the good high frequency response of the sensors, the PCB132s are able to measure second-mode waves. They have been shown to have a flat response to 300 kHz.[19] However, the sensors were designed as time-of-arrival sensors and have not yet been accurately calibrated for instability measurements. The calibration uncertainty affects the amplitude of fluctuation measurements, but is unlikely to affect frequency measurement. In addition, there is some uncertainty about the spatial resolution of the sensors. The sensor diameter is 3.18 mm, but the sensing element is a 0.762×0.762-mm square. The surface of the sensor is coated with a conductive epoxy. It is uncertain how pressure is transmitted to the sensing element through this epoxy, so the active sensing area is unknown. It has been stated earlier that the sensing element size was 1×1.6-mm,[18–22] but further communication with PCB revealed that to be an error.

In order to compare the measured second-mode wave frequencies to computations, power spectral densities were calculated from the PCB132 data. The PCB132 time traces were first normalized by the boundary-layer edge pressure, taken from the Taylor-Maccoll solution for a sharp cone. The power spectral densities were then calculated for record durations up to 0.75 seconds using Welch's method. The records were shorter if the run time was less than 0.75 seconds, with the shortest record being 0.42 seconds. A Blackman window of 1000 points was used, with 50 points of overlap between each window and the next. For each run, approximately 1560 to 3900 FFTs were averaged. The frequency resolution for each PSD is between 2 and 5 kHz. The variation is due to the varying sampling rates that were used, and does not appear to affect the resulting spectra.

Pressure fluctuations with frequencies between 0 and 50 kHz were measured with Kulite XCQ-062-15A sensors and one Kulite Mic-062 sensor. The low-frequency pressure fluctuations measured by the Kulites peak near the end of transition.[23–27] The location of this peak can be compared to N factor computations from STABL, as well as transition location as measured by thermocouples.

Kulite pressure transducers use silicon diaphragms as the basic sensing mechanisms. Each diaphragm contains a fully active four-arm Wheatstone bridge. The Kulites have screens to protect the diaphragms

American Institute of Aeronautics and Astronautics

from damage. The sensors used had A-type screens, which have a large central hole. This screen offers only a small amount of diaphragm protection, but gives a flatter frequency response. The sensitive area of the A-screen sensor is the hole size (0.81 mm^2).

The Mic-062 Kulite microphone measures the pressure differential across a diaphragm up to ± 7 kPa. The back side of the diaphragm has a pressure reference tube that is approximately 0.05 m long. This tube was bent 90 degrees to fit inside the model and left open to the plenum inside of the model. The plenum gives an approximately steady reference pressure, and high frequency components of this pressure are filtered by the long reference tube. The repeatability of the sensors is approximately 0.1% of the full scale (7 Pa).

The XCQ-062-15A sensors measure absolute pressure between 0 and 103 kPa. They are mechanically stopped above 103 kPa to prevent damage to the diaphragms at high pressures. Because of their larger measurement range, the sensors are less sensitive than the Mic-062's. However, they have a higher nominal resonant frequency of 225 kHz. The repeatability of the sensors is approximately 0.1% of the full scale (0.1 kPa).

D. Data Acquisition

Two data acquisition systems were used with the pressure sensors in order to obtain a comparison between the two for future tests. Both systems provide high-speed sampling and anti-aliasing over many channels. Table 2 shows which sensors were run on each system at each facility, except for the 12 thermocouples in the third row, which were run through the Tunnel 9 DARE 9 (Data Acquisition and Recording Equipment) data system. On this system, data was sampled at 500 Hz and analog filtered with a 30-Hz low-pass Butterworth filter with 6 poles. The data were digitally filtered forward and backward to avoid introducing any time delay. The digital filter cutoff frequency varied between 3 and 13 Hz, increasing with unit Reynolds number.

Pitot-probe data in Tunnel 9 were collected using the Tunnel 9 high speed data system, which is a HBM Genesis 5i with 15-bit resolution. The sampling rate was 1 MHz. The Kulites were low-pass filtered at 25 kHz, and the PCB132 sensors were low-pass filtered filtered at 250 kHz. For the first 7 runs in the Langley Mach 6 tunnel, the same setup was used as in the Langley Mach 10 tunnel. After that point it was changed to what is noted in the table.

Location	Tunnel 9	LaRC Mach 6	LaRC Mach 10
1A	Sandia	Sandia	Purdue
2A	Sandia	Sandia	Sandia
3A	Sandia	Sandia	Sandia
4A	Sandia	Sandia	Sandia
5A	Purdue	Purdue	Purdue
6A	Sandia	Sandia	Sandia
7A	Sandia	Sandia	Sandia
8A	Sandia	Purdue	Sandia
1B	Purdue	Sandia	Purdue
2B	Purdue	Purdue	Purdue
3B	Sandia	Sandia	Sandia
4B	Sandia	Sandia	Sandia
5B	Sandia	Sandia	Sandia
6B	Sandia	Sandia	Sandia
7B	Sandia	Sandia	Sandia
8B	Purdue	Purdue	Sandia

Table 2: Data Acquisition Layout

1. Purdue System

The PCB132 sensors all are powered by a PCB 482A22 signal conditioner that provides constant-current excitation to the built-in sensor amplifier. The constant current can be varied from 4 to 20 mA; 4 mA was used for all measurements. The signal from the Kulite pressure transducers is processed by custom-built electronics, which also supply a 10 V excitation. The output signal is amplified by a gain of 100 with an INA103 instrumentation amplifier to give the DC signal. One Tektronix DPO7054 Digital Phosphor Oscilloscope was used for data acquisition with this system in Tunnel 9. A Tektronix DPO7104 Digital Phosphor Oscilloscope was used at NASA Langley. The oscilloscopes have built-in digital filtering, so separate anti-aliasing filters are not required. The DPO7054 has a system bandwidth of 500 MHz and an 8-bit vertical resolution. The resolution can be increased to over 11-bit in Hi-Res mode. Hi-Res mode is used to increase the vertical resolution and reduce random noise. In this mode, the oscilloscopes sample at the maximum sampling rate and then average in real time and save the data at the specified sampling rate. The DPO7104 has similar capabilities, but less memory. Five seconds of data were recorded for each run. The sampling rate of the oscilloscope was 5 MHz at Tunnel 9, and 2 MHz at NASA Langley.

2. Sandia System

As with the Purdue system, the PCB sensors connect to a PCB 482A22 signal conditioner. The output from the signal conditioner is fed through a Krohn-Hite Model 3944 Filter with a 1 MHz low-pass anti-aliasing Bessel filter. This filter has four poles and offers 24 dB of attenuation per octave. The sampling frequency for the PCB132 sensors was 2.5 MHz.

A 10 V excitation is applied to the Kulites using an Endevco Model 136 DC Amplifier. The amplifier was also used to supply a gain of 100 for Kulite signal output. A Krohn-Hite Model 3384 Tunable Active Filter was used as a 200 kHz anti-aliasing low-pass Bessel filter for the Kulites. The filter has eight poles and provides 48 dB attenuation per octave. The Kulite sampling frequency was 1 MHz. One E-type Medtherm thermocouple using an Omega cold junction was also processed through the same system, except that the filter was set to 20 Hz. Data were acquired using a National Instruments PXI-1042 chassis with 14-bit PXI-6133 modules (10 MHz bandwidth) for data acquisition. Data were acquired for 0.75 seconds during the constant-condition portion of each wind-tunnel run. With the settings used here, this sample length fills the memory of the system. The hot films were run using a custom-built constant-temperature anemometer. The signal from the hot films was filtered in the same way as the Kulites.

III.   Stability Computations

The STABL software suite from the University of Minnesota was used to compute the growth of the second-mode waves. The laminar mean flows were solved as full Navier-Stokes solutions using an optimized 2D/axisymmetric solver based on the implicit Data-Parallel Line Relaxation (DPLR) method[28] which is provided with the stability code STABL.[29] The solver produces second-order accurate laminar flow solutions with shock capturing and low dissipation. The geometry was a 7° half-angle sharp cone that was 0.517 m long at zero angle of attack. For each of the simulations, 300×350 structured grids were generated with clustering both at the body surface and nose tip.

The flow for NASA LaRC cases is considered to be a non-reacting mixture of 76.7% N_2 and 23.3% O_2 by mass. The flow for the AEDC Tunnel 9 cases is considered to be non-reacting pure N_2. Free-stream conditions were provided by the tunnel operators for each specific experiment. For the NASA LaRC cases, the species viscosities were specified in a general fashion so that different viscosity models could be used through specified temperature ranges. Blending functions were used to maintain smooth function values and derivatives between models. Sutherland's viscosity law was used for temperatures up to 1550 K and Blottner's viscosity model was used for temperatures higher than 1600 K. Both viscosity models used the coefficients for air. For the AEDC cases, the calibrated N_2 viscosity model for Tunnel 9 was used.[30]

The linear PSE and LST analyses were performed using the PSE-Chem code which is distributed as a part of the STABL suite.[29] For the LST analysis, a parallel flow assumption was made by neglecting derivatives of mean flow quantities in the direction of the computational coordinate along the body. Spatial amplification rates and N factors were found for given disturbance frequencies and surface locations. More details about the linear PSE approach used in STABL can be found in Reference 29.

American Institute of Aeronautics and Astronautics

IV.   Results

A.   Summary of Data Obtained

A large data set was obtained during these tests, and not all of it is presented in this paper. Much analysis remains to be completed, the results of which are to be published in the future.[31] In particular, the data taken at NASA LaRC using roughness elements, blunt nosetips, and angle of attack have not yet been examined in detail. Table 3 summarizes the data obtained in each tunnel. A total of 67 runs were made with the cone, with an additional 10 runs made in the Langley Mach 6 tunnel taking Pitot acoustic noise measurements with a Kulite. Pitot noise measurements were made for all runs in Tunnel 9, including seven runs which used a PCB132 sensor to make noise measurements.

	Tunnel 9 (Mach 10)	Langley Mach 10	Langley Mach 6
Sharp Cone, Re/m	2.0–6.6,13.5, $30{\times}10^6$ (12)	$1.7 - 6.7{\times}10^6$ (10)	$4.9 - 19.9{\times}10^6$ (12)
Pitot Probe, Re/m	2.0–6.6,13.5, $30{\times}10^6$ (12)	None	$7.1 - 22.3{\times}10^6$ (10)
Roughness (mm)	None	$0.114 - 0.673$ (11)	$0.178 - 0.343$ (5)
Blunt Nose (mm)	None	0.508 (4), 1.52 (3)	None
AoA	0°	0°	0°, 2.13° (4), 3.09° (2)

Table 3: Summary of data obtained in each tunnel. Numbers in parentheses show the total number of runs in that category. Dashes indicate many values within a range were used.

B.   Detection of Second-Mode Waves

Second-mode waves were successfully observed in all three tunnels using the PCB132 sensors. They were also observed using optical methods in Tunnel 9.[32] This is the first time that instability waves have been measured in these tunnels. Waves were detected in linear and non-linear stages of growth, as well as during breakdown.
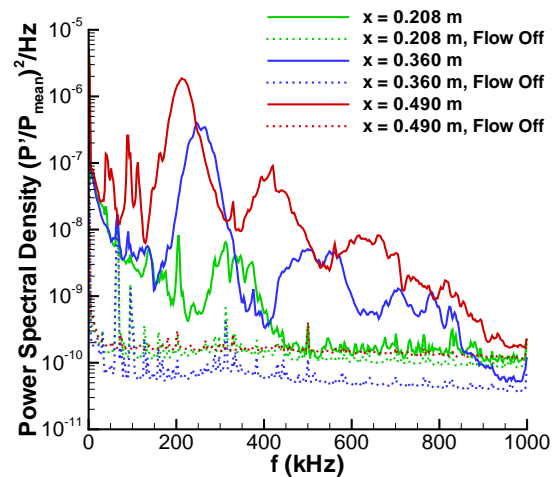

Figure 5: Comparison of measured PSD with flow on and flow off. Tunnel 9, $Re/m = 6.5 \times 10^6$.

Second-mode waves appear as peaks in the PSD plots. Figure 5 shows power spectra at different positions on the cone both with and without flow. The second-mode waves are the large, broad peaks below 400 kHz. As x increases, the peaks become larger, showing that the waves are growing with x. In addition, the frequencies decrease, due to the boundary layer becoming thicker. The second-mode wavelength grows with the boundary layer, causing the second-mode frequency to decrease.[1] The higher-frequency peaks are harmonics of the second-mode waves, showing that the waves have become nonlinear by $x = 0.360$ m. The power spectra taken without flow show background electronic noise, which falls to low, nearly constant levels

by 50 kHz. Since the second-mode peaks do not appear without flow, they are unlikely to be due to electronic noise.

Also apparent are the low-frequency fluctuations in the boundary layer not due to second-mode waves. These can be seen most clearly at $x = 0.208$ m at frequencies below 300 kHz. The measured fluctuations are substantially higher than the electronic noise, showing that they are due to the flow. These fluctuations decrease with frequency, eventually disappearing into the electronic noise. The second-mode waves rise out of these background fluctuations, which is why the visible peaks generally end at lower amplitudes than they begin.

1. Comparison of Measured Spectra with Computed N Factors

Figure 6 shows comparisons of measured power spectra with computed N factors. N factor corresponds roughly with wave amplitude, since it is a representation of how much the wave has grown. Different disturbance frequencies amplify at different rates throughout the boundary layer, so N factor varies with frequency. STABL computes N factors for discrete frequencies, which are plotted here. The N factor scales have been arbitrarily adjusted so that the maximum N factor matches the maximum PSD value. They are matched only to make comparison easier, since without knowing the initial amplitude, the N factors cannot be used to compute amplitudes.

If the computations are accurate and the measurements detect second-mode waves, peaks should be evident at the same frequencies in both the measurements and the computations. The measured peaks line up well with the predicted second-mode frequencies, showing that the measured peaks are second-mode waves. Agreement between the spectra at $\phi = 0°$ and $\phi = 120°$ is also fairly good, indicating good flow axisymmetry.

Figure 6a shows linear waves, evident from the presence of a single peak. Figure 6b shows nonlinear waves, evident from the presence of multiple higher-frequency peaks, which are the harmonics of the second-mode waves. Figure 6c shows nonlinear waves in a later stage of development, where the harmonics have become less apparent as the higher frequency fluctuation levels increase. The measured and computed frequencies compare well whether or not the waves are linear. The shapes of the peaks also generally match well, though Figure 6c shows a wider measured peaks than what is computed. This is likely due to nonlinear effects which cause the peak to broaden as the waves saturate and break down. This process is not accounted for in the theory, so the computations are not able to reflect it. Theory also does not account for the harmonics, which is why they do not appear in the N factor curves.

Many more comparisons of this type are possible with this data set. Five unique conditions were run in Tunnel 9, 7 were run in the Langley Mach-10 tunnel, and 8 were run in the Langley Mach-6 tunnel. In most of the data, waves are visible at two axial locations. If computations were available for all 20 of the unique conditions, approximately 40 of these comparisons could be made, without taking into account the data using roughness elements and blunt nosetips.

### 2. Growth of Second-Mode Waves with Unit Reynolds Number

Plots of spectra at different unit Reynolds numbers in each of the tunnels show wave growth and breakdown (Figure 7). Second-mode waves are again evident,with frequencies that rise as the boundary layer thins with increasing unit Reynolds number. Turbulence is apparent at some of the higher Reynolds number conditions. A turbulent spectrum exhibits elevated fluctuations at all frequencies, with no second-mode peak visible. An example of a turbulent spectrum is seen in Figure 7a at $Re/m = 13.3 \times 10^6$. Data from $x = 0.360$ m are plotted in Figure 7 because all of the types of waves that were observed were seen at that position. Data from $x = 0.208$ m and $x = 0.490$ m also show waves in multiple stages of growth, but waves were not visible for as many conditions at these locations. At $x = 0.208$ m, the waves are often too small to observe, and at $x = 0.490$ m, the flow has often become turbulent.

In the Langley Mach-6 tunnel, waves are observed at all tested Reynolds numbers on some but not all sensors. Transition appears on the PCBs for $Re/m > 6.66 \times 10^6$. It is inferred that transition has occurred when laminar spectra are evident on at least one sensor, but turbulent spectra are observed on sensors farther downstream. Linear waves are seen at the lowest Reynolds number condition, and larger, nonlinear waves at the next condition, showing growth with unit Reynolds number. At the rest of the conditions, the waves have saturated and begun to break down. The second-mode peak flattens out and disappears as the waves break down, and the low-frequency pressure fluctuations increase. In the late stages, the peak seems to be

American Institute of Aeronautics and Astronautics
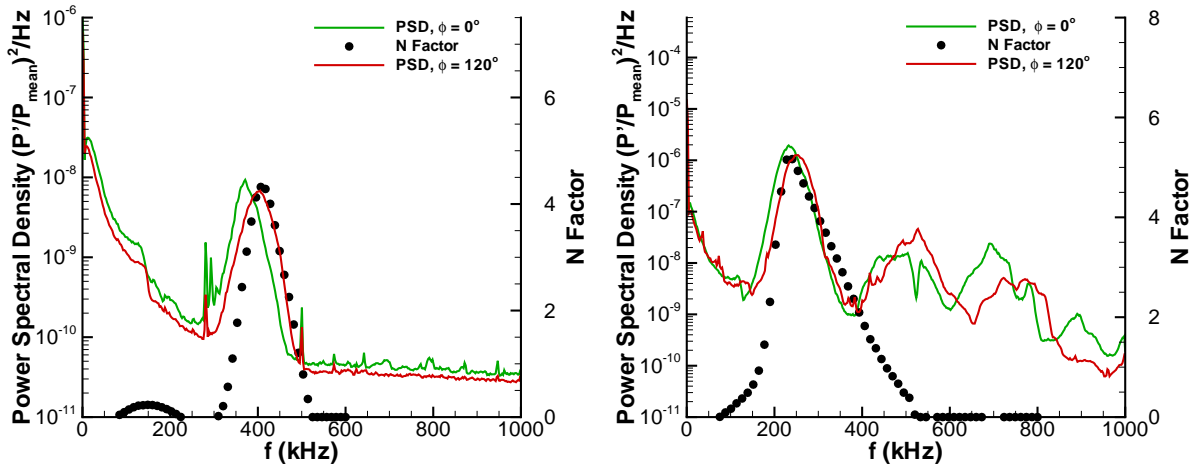
(a) Langley Mach 6, $Re/m = 9.4 \times 10^6$, $x = 0.208$ m.

(b) Langley Mach 10, $Re/m = 6.6 \times 10^6$, $x = 0.360$ m.
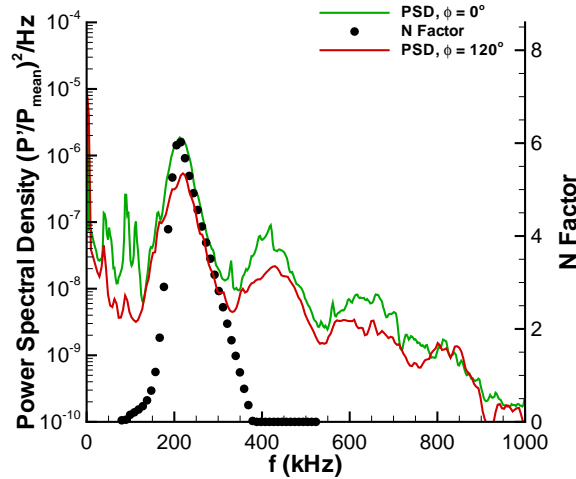
(c) Tunnel 9, $Re/m = 6.5 \times 10^6$, $x = 0.490$ m.

Figure 6: Comparisons of STABL computations to PCB132 measurements.

superimposed on a turbulent spectrum, and changes in amplitude are not evident at frequencies both higher and lower than the second-mode waves. The cause of the peak near 550 kHz is unknown.

In the Langley Mach-10 tunnel, waves are observed at all tested Reynolds numbers on at least some sensors. Transition is not observed on the PCBs in this tunnel, since a broad spectrum without a second-mode peak is not evident at the maximum unit Reynolds number. The growth of the second-mode waves and their harmonics can be clearly seen as unit Reynolds number increases. The second-mode peaks increase in both height and width with increasing unit Reynolds number. Linear waves are present at $Re/m = 1.7 \times 10^6$, and a single harmonic has appeared by $Re/m = 3.4 \times 10^6$. For all subsequent conditions, three peaks are visible, indicating two harmonics.

In Tunnel 9, waves can be seen at $x = 0.360$ m from $Re/m = 2.2 \times 10^6$ to 13.5×10^6. Instead, a turbulent spectrum is seen. Again, the waves at the lowest condition, seen near 125 kHz, are linear. At $Re/m = 3.8 \times 10^6$, the electronic noise level was elevated for an unknown reason. This run was the first run performed, and it was the only run to exhibit such elevated noise levels. However, the second-mode waves are still visible at about 200 kHz. The waves are nonlinear at the next condition, $Re/m = 6.5 \times 10^6$, with three peaks visible. At $Re/m = 13.5 \times 10^6$, the waves are still visible, but breakdown has begun. This is

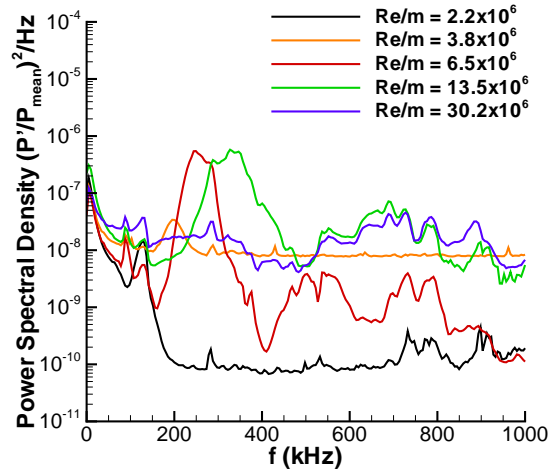American Institute of Aeronautics and Astronautics

shown by the elevated low-frequency fluctuations, as well as the disappearance of the harmonics. A turbulent spectrum is observed at $Re/m = 30.2 \times 10^6$.
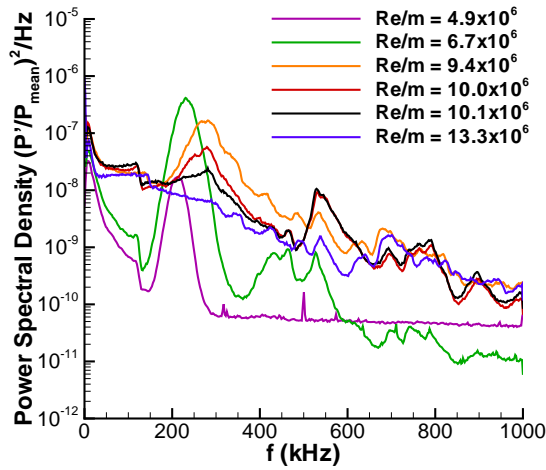
(a) Langley Mach 6, $x = 0.360$ m, $\phi = 0°$. Data for $Re/m = 4.9 \times 10^6$ is from $\phi = 120°$.
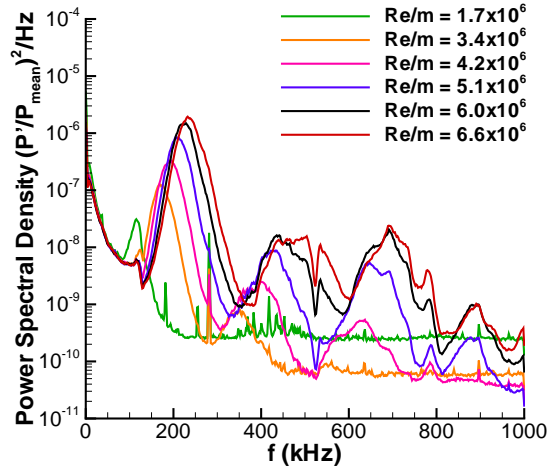
(b) Langley Mach 10, $x = 0.360$ m, $\phi = 0°$.

(c) Tunnel 9, $x = 0.360$ m, $\phi = 0°$.

Figure 7: PCB measurements at representative unit Reynolds numbers in the different tunnels.

American Institute of Aeronautics and Astronautics

C. Examination of Second-Mode Wave Amplitudes

Wave saturation and breakdown is difficult to detect by looking at the spectra, since the amplitude of the waves is related to the integral of the second-mode peak, and not just the height of the peak. Computations of wave amplitude based on PCB132 measurements are not yet quantitatively accurate, as mentioned earlier. However, it seems reasonable to expect the amplitudes to be useful in a qualitative sense.

RMS amplitudes of the second-mode waves were computed by integrating under the second-mode peak using a trapezoidal integration scheme and taking the square root of the result. The lower frequency bound for this integral was found by visually locating the lowest frequency of the second-mode peak. The higher bound was chosen as the frequency at which the power spectral density was again equal to the value at the lower bound. For instance, in Figure 6b for $\phi = 120°$, the lower bound is where the peak is first visible, at 148 kHz. To find the higher bound, a horizontal line is followed from the point where the peak appears to the point where it again intersects the curve, which is at 353 kHz. This interval covers the majority of the visible peak. In a case like the spectrum for $\phi = 120°$ in Figure 6c, where the first peak clearly ends before the horizontal line again intersects the curve because two peaks have merged together, the higher bound was chosen as the point at which the local minimum between the two peaks occurred. Finding the lower bound visually is not necessarily the most accurate method, but the effect on the computed amplitude is small. The PSD is plotted on a logarithmic scale, and the value at the lower bound of the peak is typically one or two orders of magnitude lower than the maximum. No amplitudes were calculated for spectra in which a second-mode peak was not clearly visible.

Figure 8 shows the wave amplitudes in both of the Langley tunnels plotted against the freestream unit Reynolds number. The amplitude curves tend to shift up with increasing axial position, as would be expected. This is because the waves are growing with downstream position, so they reach a given amplitude at lower unit Reynolds numbers as streamwise position increases. However, more measurements are required to determine if the amplitude curves from each sensor location have the same shape.

In general, the wave amplitudes increase with unit Reynolds number. However, in some cases the amplitudes reach a maximum and then begin to decrease. This indicates that the waves have saturated and then begun to break down. Breakdown is inferred when the wave amplitudes decrease with unit Reynolds number, and so the point at which breakdown begins is the point at which the slope of the amplitude curve first becomes negative. Saturation is inferred when the wave amplitude stops growing with unit Reynolds number. The saturation amplitude is different on each sensor, which may be due to calibration inaccuracies, real differences in saturation amplitude, or both.
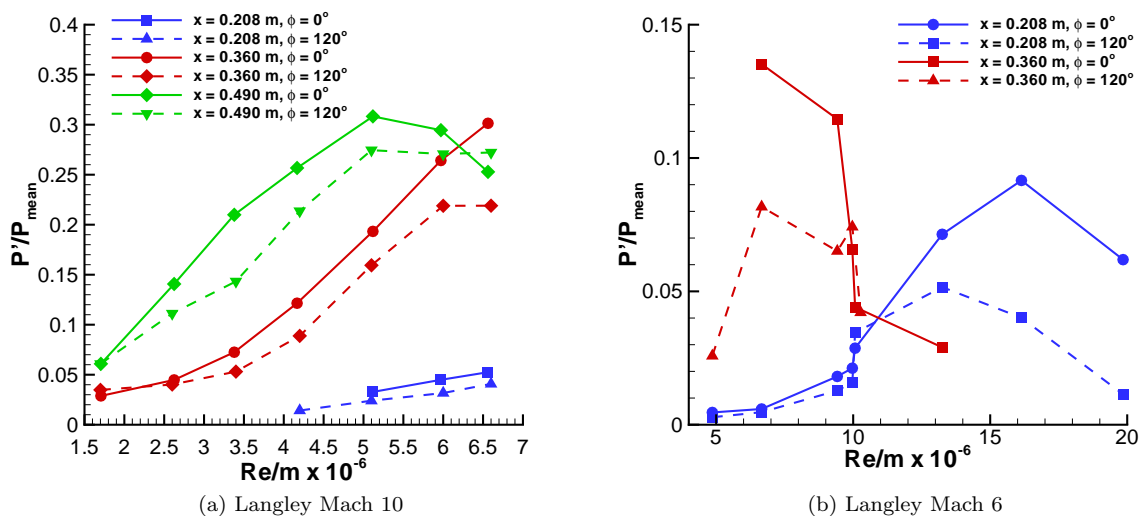

(a) Langley Mach 10

(b) Langley Mach 6

Figure 8: Second-mode wave amplitudes calculated from the PCB132 data in the Langley tunnels. Note that since the calibration of the sensors is uncertain, comparison of amplitudes is difficult, especially between different sensors.

1. Amplitudes in the 31-Inch Langley Mach 10 Tunnel

In the Langley Mach-10 tunnel (Figure 8a) amplitudes at $x = 0.490$ m, $\phi = 0°$ are observed to approach a maximum value of about 30% of the mean, and then begin to break down. The amplitudes at $x = 0.490$ m, $\phi = 120°$ do not decrease, but the power spectra show broadband frequency filling, indicating breakdown. Breakdown is not observed at the other two positions. However, saturation occurs at $x = 0.360$ m, $\phi = 120°$ at amplitudes near 20%. The amplitudes at $x = 0.360$ m, $\phi = 0°$ reach near 30%. This is similar to the saturation amplitudes observed at $x = 0.490$ m, but it is not clear how close the waves are to saturating at this position, so the saturation amplitudes may be different.

At $x = 0.490$ m, breakdown begins at $Re/m = 5.1 \times 10^6$. Computations are not yet available at this condition, so the N factor at which the waves begin to break down is unknown. However, computations are available at $Re/m = 4.2 \times 10^6$, as well as $Re/m = 6.6 \times 10^6$, so a range for the N factor can be found. Finding the computed N factor at $x = 0.490$ m at each of these conditions puts breakdown between $N = 4.75$ and $N = 6.20$. Using a linear interpolation, the N factor at this location for $Re/m = 5.1 \times 10^6$ is found to be 5.3. Therefore, the N factor at the beginning of breakdown for this case, is between $N = 4.75$ and $N = 6.20$, and is likely higher than 5. This is near the expected N factor range for transition onset. However, turbulent spectra were not observed with the PCB132 sensors in the Langley Mach-10 tunnel, so the N factor at transition could not be measured.

2. Amplitudes in the 15-Inch Langley Mach 6 Tunnel

In the Langley Mach-6 tunnel, the beginning of breakdown is observed at $x = 0.208$ m for both rows of sensors. At this location, the saturation amplitudes are about 5% and 9%. Breakdown seems to begin at a lower Reynolds number for $\phi = 120°$ than $\phi = 0°$, suggesting that there may be a real difference in saturation amplitude between the two rays. The cause of this asymmetry is unknown. Computations are not yet available at high enough Reynolds numbers to determine at what N factor breakdown is observed at this position.

Some later part of the breakdown process is visible at $x = 0.360$ m at $\phi = 0°$. Higher amplitudes around 14% are reached at that location, and the amplitudes decrease with unit Reynolds number. This indicates that the waves have already saturated at $Re/m = 6.7 \times 10^6$ and are breaking down. However, the amplitudes at $x = 0.360$ m, $\phi = 120°$ show growth, saturation, and breakdown. Growth is evident at $\phi = 120°$ and not $\phi = 0°$ because data at the lowest run condition, $Re/m = 4.9 \times 10^6$, were not recorded for $\phi = 0°$. The waves appear to saturate at 7-8%, but the dip in the middle of the peak in amplitudes casts doubt on the reliability of these data. It is unknown why this dip is present. Since it is uncertain at what condition breakdown begins at this position, the N factor at which breakdown occurs cannot be determined.

The saturation amplitude at $x = 0.360$ m is much higher than those observed at $x = 0.208$ m. The discrepancy may be due to calibration inaccuracy, though it is also possible it is due to different spatial averaging. Spatial averaging becomes important when the sensor size is significant with respect to the wavelength, which is the case for these measurements. Since the boundary layer is thicker at positions farther downstream, and the second-mode wavelength is dependent on the boundary layer thickness, less spatial averaging would be expected at $x = 0.360$ m than at $x = 0.208$ m. This would tend to cause measured amplitudes to be larger at $x = 0.360$ m, as observed. Approximating the second-mode wavelength as twice the boundary layer thickness, and using 0.762 mm as the sensor length, the wavelength is found to be 2.7 times the sensor length at $x = 0.208$ m and 3.5 times the sensor length at $x = 0.360$ m. This is a 30% increase, which could produce a noticeable difference in measured amplitudes.

Due to the lower number of runs, amplitude data in Tunnel 9 is too sparse to plot against unit Reynolds number. However, amplitudes up to 30% are observed, which agrees with the Langley data. It is unknown if this is the maximum wave amplitude for Tunnel 9.

Breakdown and saturation occur at lower amplitudes in the Langley Mach-6 tunnel than in Tunnel 9 at Mach 10 and the Langley Mach-10 tunnel. An increase in maximum wave amplitude with Mach number was also observed in Reference 18. In those experiments, breakdown amplitudes increased from 1.4% at Mach 5 to 12% at Mach 6 and 24% at Mach 8. The 12% amplitude at Mach 6 is within the range of the breakdown amplitudes observed in the Langley Mach-6 tunnel. Amplitudes also seem to increase from the Mach 8 result in Reference 18 to the Mach 10 results here, though the difference is not large enough to be certain.

American Institute of Aeronautics and Astronautics

D.   Comparison of Langley Mach 10 Data and Tunnel 9 Data

The Reynolds numbers match closely between the Langley and Tunnel 9 Mach 10 tests at one condition ($Re/m = 6.6 \times 10^6$ and 6.5×10^6, respectively). The flow does not match exactly, which is reflected in the slightly different computed N factors (Figure 9), as well as the slightly different Reynolds numbers. The stagnation conditions in Tunnel 9 were $P_0 = 8.63 \times 10^3$ kPa and $T_0 = 1000$ K , and the stagnation conditions in Langley were $P_0 = 1.00 \times 10^4$ kPa and $T_0 = 1002$ K. The temperature ratio T_e/T_w is slightly lower in Langley than in Tunnel 9, 0.23 compared to 0.25. The ratios of the measured amplitudes in Langley to those in Tunnel 9 can be compared to the amplitude ratios computed by STABL.

Figure 10a shows the measured amplitudes for the matching conditions in both Tunnel 9 and the Langley Mach 10 tunnel. In both tunnels, the amplitudes increase more slowly as x increases for $\phi = 120°$. However, in Tunnel 9 at $\phi = 0°$, the amplitudes grow linearly with x. In the Langley Mach-10 tunnel at $\phi = 0°$, the waves grow from $x = 0.208$ m to $x = 0.360$ m, and then decrease from $x = 0.360$ m to $x = 0.490$ m, indicating that breakdown occurs between these last two positions. The amplitudes in Tunnel 9 are almost always lower than those measured in Langley, and the amplitudes at $\phi = 120°$ are generally lower than those at $\phi = 0°$ in both tunnels. The one exception to both of these trends is at $x = 0.490$ m, where the waves are breaking down in the Langley Mach-10 tunnel at $\phi = 0°$. The waves are inferred to be breaking down at this point because the wave amplitudes are decreasing with both axial position and unit Reynolds number (Figure 8a). Since the waves in Langley had been larger than those in Tunnel 9, it makes sense that breakdown would be observed earlier in Langley than in Tunnel 9.

There is a large amplitude difference between the two azimuthal locations at $x = 0.490$ m in Tunnel 9. This might suggest that saturation or breakdown occurred earlier for $\phi = 120°$. The lack of growth between $x = 0.360$ m and $x = 0.490$ m at $\phi = 120°$ could be explained by saturation, since the amplitude would not increase past the saturation amplitude. If the waves were breaking down at $\phi = 120°$, that would imply that larger amplitudes had been reached in between the two sensors, but breakdown had caused a decrease in amplitude before $x = 0.490$ m.

It is unknown whether or not the waves are saturated or breaking down at this condition in Tunnel 9. The spectra at $x = 0.490$ m in Tunnel 9 are shown in Figure 10b. The fluctuations are generally higher at $\phi = 0°$, but otherwise the spectra look similar. The peaks are more distinct at $\phi = 0°$, especially the third peak near 600 kHz. The shape of the spectrum at $\phi = 120°$ is similar to other spectra in the early stages of breakdown, but without more data at similar conditions, it is difficult to classify.
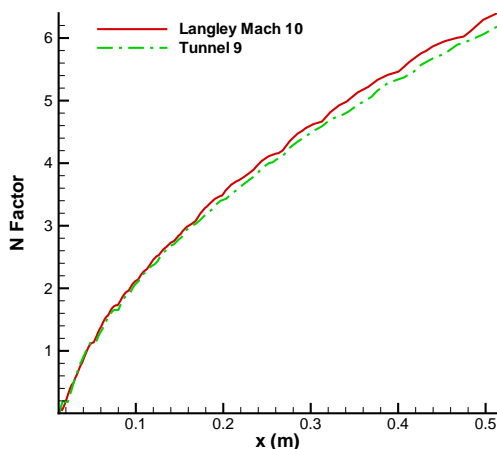

Figure 9: Comparison of the computed maximum N factor along the cone in Tunnel 9 and the Langley Mach 10 tunnel at $Re/m = 6.5$ and 6.6×10^6, respectively.

A difference in saturation or breakdown amplitude in Tunnel 9 between the two azimuthal positions might be explained by tunnel noise. Since the cone was mounted off-center, the sensors at $\phi = 120°$ were closer to the tunnel wall. This may have exposed them to a higher freestream noise level, which might cause saturation and breakdown to occur earlier.

American Institute of Aeronautics and Astronautics
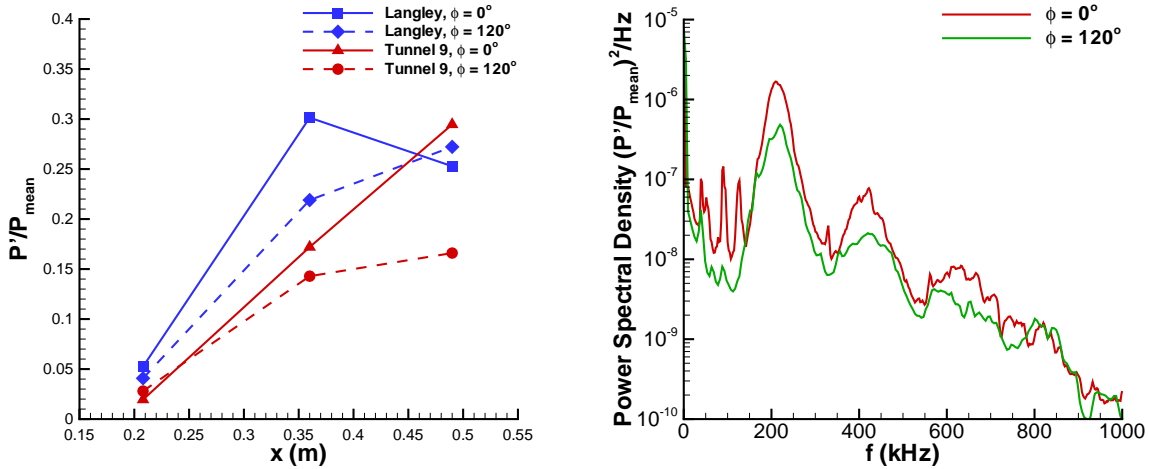
(a) Comparison of measured amplitudes between Tunnel 9 and the Langley Mach 10 tunnel at $Re/m = 6.5$ and 6.6×10^6, respectively.

(b) PCB spectra at $x = 0.490$ m in Tunnel 9. $Re/m = 6.5 \times 10^6$.

Figure 10

In general, the ratios between the amplitudes in Langley and the amplitudes in Tunnel 9 are larger than predicted by STABL. This may be due to calibration errors in the sensors. However, it may also suggest that freestream noise levels are causing larger waves in Langley than in Tunnel 9. Since the Langley Mach-10 tunnel has a smaller cross-section, the freestream noise levels should be higher.[33] The ratios computed by STABL do not account for differences in A_0, which might be caused by different freestream noise levels. If higher freestream noise levels in the Langley Mach-10 tunnel lead to higher values of A_0, the waves would be larger in that tunnel than in Tunnel 9, as was observed.

E. Effect of Record Length on Second-Mode Wave Measurements

While the tunnels in which the current tests have been performed have run times on the order of 1-10 seconds, many hypersonic tunnels have much shorter run times. The issue of how long a record needs to be in order to detect second-mode waves is important if measurements are desired in such a tunnel. Figure 11 shows power spectra from Tunnel 9 at $Re/m = 2.2 \times 10^6$. Because this is a relatively low Reynolds number, the waves observed are weak and have a low frequency. Both of these factors should make them harder to detect as record length decreases, making these results conservative. The power spectra have been found for records of varying lengths originating at $t = 2.25$ seconds. Blackman windows of 400 data points were used, with 50 points of overlap. At the 5 MHz sampling rate, this corresponds to windows of 80 μs. The frequencies observed at this condition are about 130 kHz and 110 kHz, so an 80 μs record can contain up to 10 or 9 wave cycles, respectively. The shortest interval is a single FFT. For 1 ms intervals, 15 FFTs are averaged, and for 3 ms intervals, 43 FFTs are averaged. The frequency resolution of the resulting PSD data is 9.75 kHz. The longest interval is 0.75 seconds long. This interval was processed in the same manner as the rest of the data in this paper.

At $x = 0.360$ m, the second-mode waves at 130 kHz are visible for all record lengths. However, the amplitudes of the waves change with record length. This is also observed at $x = 0.490$ m. In fact, for the single FFT, the waves are hardly visible at $x = 0.490$ m.

The cause of this effect is the differing amount of averaging as the record length changes. Since the waves originate from noise in the freestream, there is a certain amount of randomness and intermittency in the waves. As the record becomes shorter, there is less averaging. The decrease in averaging causes the amplitudes to become more random. Figure 12 shows single FFTs at $x = 0.490$ m taken from different times in the run. The second-mode peaks near 110 kHz become larger as the run progresses, indicating that the starting point chosen was a time where the waves were becoming stronger. As the record length increases,

American Institute of Aeronautics and Astronautics

more of the stronger waves will be incorporated into the average, which will result in longer record times showing stronger waves. As record time continues to increase, eventually enough averages will accumulate to eliminate the effect of the randomness in the waves, and the amplitude will stop changing with record length. For this data set, the effect of the randomness appears to be largely eliminated when the record length is 3 ms long, incorporating 43 FFTs in the average.

Second-mode waves are visible in Figure 12, but the lack of averaging results in noisy spectra. The noise in the spectra combined with the intermittency of the waves makes it difficult to use such a short record as a method of detecting waves. However, 80 μs should be an excessively short time for most applications. The waves are always detected for record lengths of 1 ms, which average 15 FFTs, and since little difference is observed for increasing record length beyond 3 ms, record lengths on the order of a millisecond that average 20–50 FFTs should be sufficient to detect waves. When possible, longer record times should be used to reduce the effect of randomness on the results.
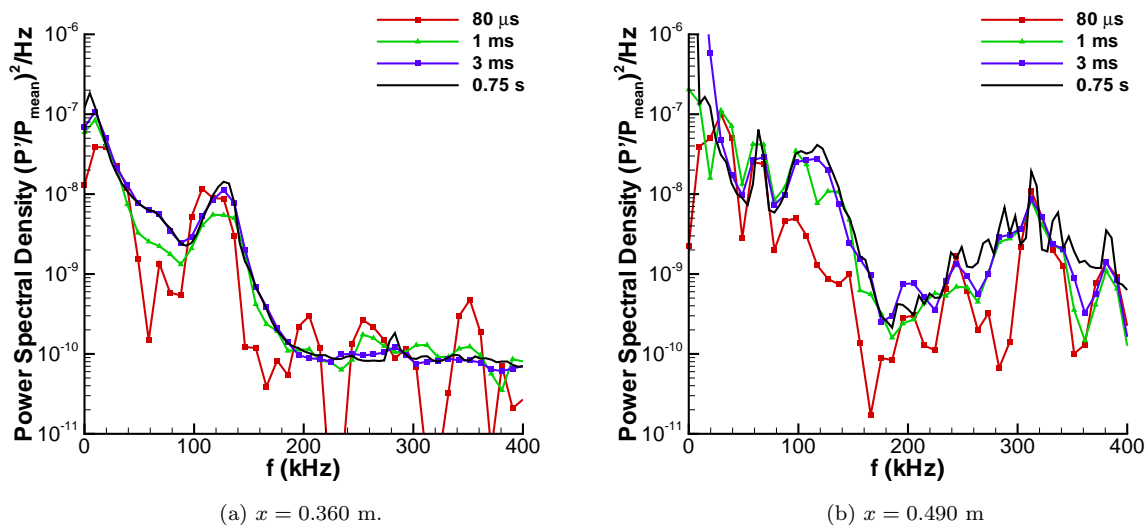

(a) $x = 0.360$ m.

(b) $x = 0.490$ m

Figure 11: Power spectra calculated from different record lengths originating at the same time in the run. Tunnel 9, $Re/m = 2.2 \times 10^6$.

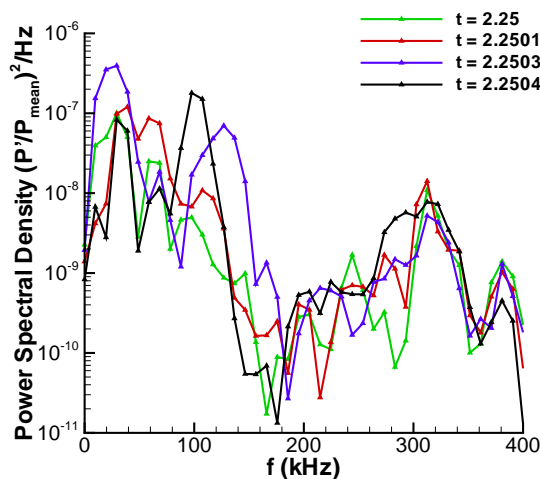Figure 12: PCB132 spectra of 80-μs-records from different times in the run. The second-mode waves are near 110 kHz. $x = 0.490$ m, Tunnel 9, $Re/m = 2.2 \times 10^6$.

American Institute of Aeronautics and Astronautics

V. Tunnel 9 Kulite Data

RMS pressure fluctuations from 0–50 kHz were calculated from Kulite measurements along the cone. These low frequency fluctuations have been shown to peak during boundary layer transition.[18, 24–27, 34] Figure 13a shows unnormalized RMS pressure fluctuations along the cone for increasing freestream unit Reynolds number. The lowest two cases show approximately constant pressure fluctuations along the cone, indicating laminar flow over the cone. The highest Reynolds number case shows a peak in the fluctuations at $x = 0.384$ m, indicating that transition occurs near this location. Figures 13b and 13c show the RMS pressure fluctuations normalized by the edge pressure and nozzle wall shear stress, respectively. The mean pressure was computed using a Taylor-Maccoll solution. The nozzle wall shear stress (τ_w) was computed using the method of Van-Driest-II. Although these quantities collapsed the RMS pressure fluctuations during previous experiments at Purdue and Sandia,[7, 18] they do not collapse the fluctuations well for this data. It is unknown why this is the case.

(a) Unnormalized Kulite RMS pressure fluctuations.

(b) Kulite RMS pressure fluctuations normalized by edge pressure.

(c) Kulite RMS pressure fluctuations normalized by wall shear stress.

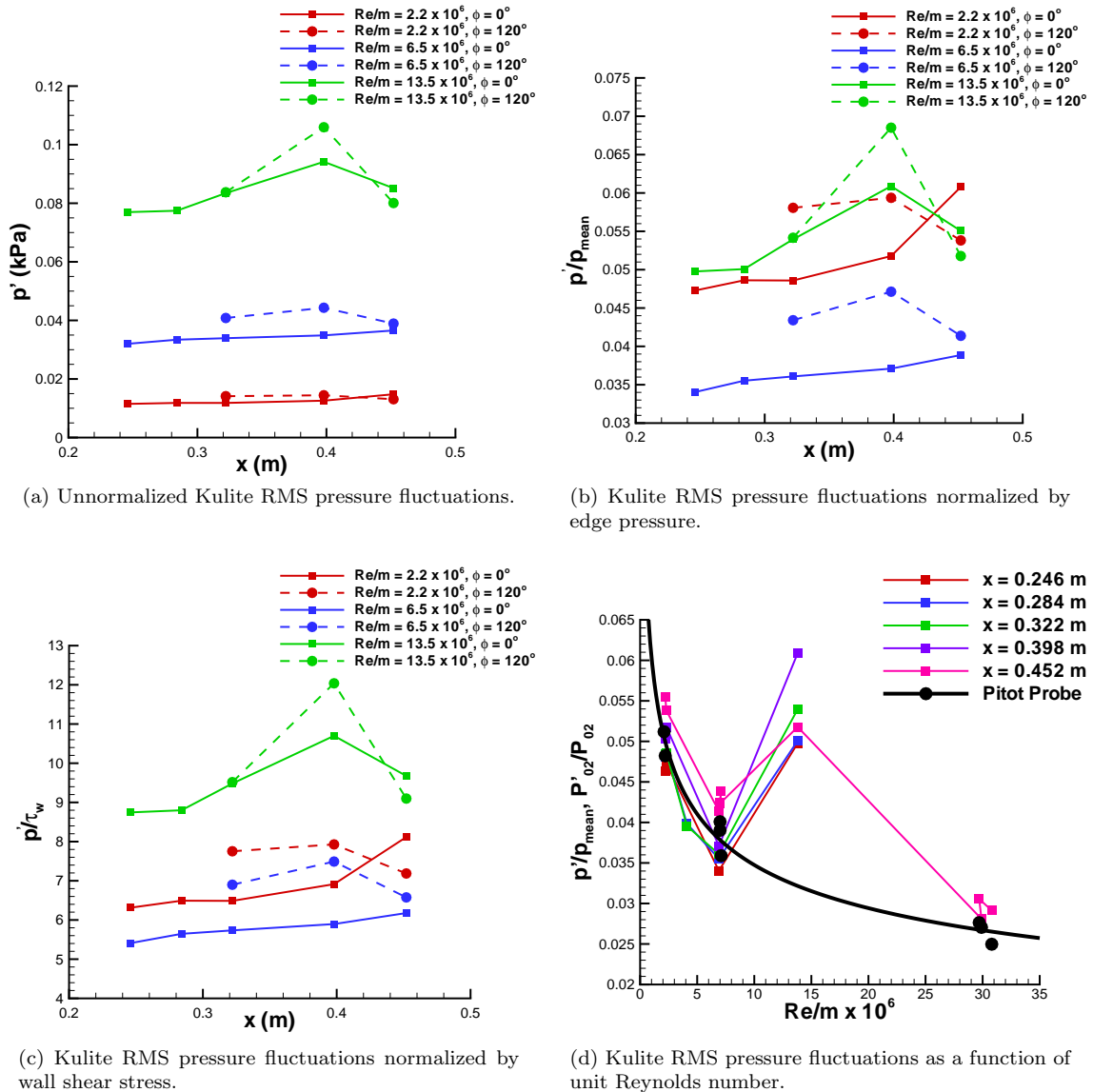(d) Kulite RMS pressure fluctuations as a function of unit Reynolds number.

Figure 13: Kulite pressure fluctuations in Tunnel 9.

The fluctuations can be compared to the tunnel noise level by plotting against the freestream unit Reynolds number (Figure 13d). The RMS pressure fluctuations between 0–50 kHz normalized by the edge

American Institute of Aeronautics and Astronautics

pressure are compared to Kulite Pitot probe noise measurements (Figure 13d). The noise level was computed by calculating the RMS Pitot fluctuations between 0 and 50 kHz and dividing by the mean Pitot pressure. A power curve fit to the Pitot noise measurements is shown to compare to the cone fluctuations. The laminar and turbulent pressure fluctuations fall onto the tunnel noise measurements. This is in agreement with previous measurements at Purdue and Sandia.[7,18] At $Re/m = 13.5 \times 10^6$, the fluctuations are elevated above the noise level. This is consistent with transitional flow measurements; however, it is unusual that all the fluctuations along the cone are above the tunnel noise level. It may be that the transition process is long in this case, causing elevated pressure fluctuations over all the Kulite transducers. More measurements are needed to confirm this.

Kulite pressure measurements were made in both the Langley 15-inch Mach-6 tunnel as well as the 31-inch Mach-10 tunnel. Unfortunately, transitional pressure fluctuation peaks were not observed in either Langley tunnel. In the 15-inch Mach-6 tunnel, transition peaks could not be clearly seen in the fluctuations along the cone, even though the second-mode waves indicated that transition was occurring over the middle of the cone. This is likely due to the sensor spacing. Additional tests are needed with smaller Kulite spacing over the middle of the cone, or a smaller Re/m spacing between runs to move the peak over the Kulites.

In the 31-inch Mach-10 tunnel, the PCB132 traces showed the growth of the second-mode waves, but not breakdown into transition. This result is consistent with the Kulite data that indicated purely laminar flow along the cone, and is also in agreement with the Tunnel 9 results at similar freestream unit Reynolds numbers.

VI. Tunnel 9 Heat Transfer Data

The row of thermocouples can be used as a reference for locating transition on the cone. The Stanton number for each thermocouple was averaged over the usable period of each run and multiplied by $Re_D^{1/2}$, where D is the base diameter of the cone. Multiplying by this Reynolds number factor collapses the Reynolds number dependence in the laminar flow data. The resulting data is plotted in Figure 14. Laminar flow is evidenced by low Stanton numbers that fall with x, and turbulent flow by high Stanton numbers that fall with x. Transitional flow is shown by Stanton numbers which rise with x.
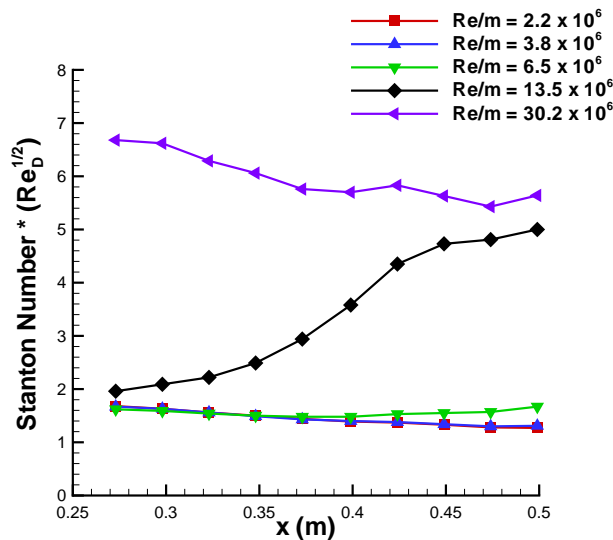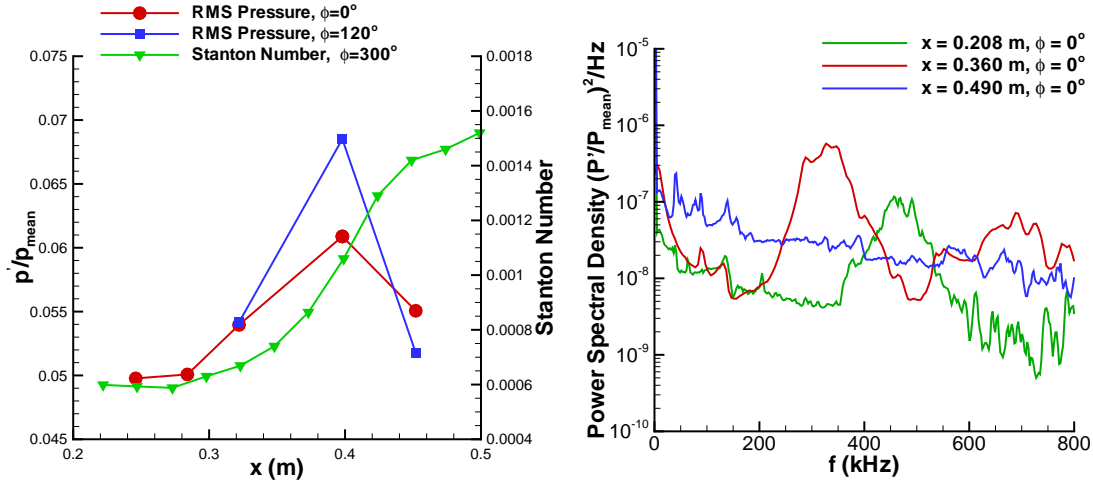

Figure 14: Stanton number along the cone in Tunnel 9.

The Kulites and thermocouples both show laminar flow for the same cases. Also, the transitional case ($Re/m = 13.5 \times 10^6$) does show the transition process occurring over nearly all of the sensors, in agreement with the Kulite data.

Figure 15a shows a comparison between the Kulite pressure fluctuations and the thermocouple data for $Re/m = 13.5 \times 10^6$. The peak in the pressure fluctuations appears midway through the rise in the Stanton number, though it is not well defined because of the sensor spacing. If thermocouples are being

American Institute of Aeronautics and Astronautics

(a) RMS Kulite pressure fluctuations compared to Stanton number along the cone. Tunnel 9, $Re/m = 13.5 \times 10^6$.

(b) Power spectra from PCB132 measurements. Tunnel 9, $Re/m = 13.5 \times 10^6$.

Figure 15: Thermocouples, Kulites and PCB132's showing transition.

used to locate transition onset, STABL computations show $N = 4.5$ at the initial rise in Stanton number at $x = 0.3$ m. If Kulites are being used to locate transition, STABL computations show $N = 5.3$ at the peak in low-frequency pressure fluctuations. PCB132 spectra from different positions along the cone are shown in Figure 15b. They show linear second-mode waves at the front of the cone, waves in breakdown in the middle (shown by the increase in low-frequency pressure fluctuations and the disappearance of harmonics), and a turbulent spectrum at the rear of the cone. This is consistent with what is shown by the Kulites and the thermocouples. In the future, additional runs near this condition would better define the relationship between peak transitional RMS pressure fluctuations and the transitional Stanton number peak.

VII.   Conclusions

Second-mode waves were successfully observed in three tunnels at multiple conditions and in varying stages of growth. Large waves with RMS amplitudes of about 20–30% of the mean pressure were observed at Mach 10, and smaller waves with RMS amplitudes up to 14% were observed at Mach 6 though the amplitudes are uncertain. The increase in maximum wave amplitude with Mach number is consistent with earlier work.[18] Wave breakdown was observed in the Langley tunnels, as shown by the saturation and decrease in wave amplitudes. The N factor at the onset of wave breakdown was estimated to be near 5 in the Langley 31-inch Mach 10 tunnel. Wave breakdown was also observed in Tunnel 9 under similar conditions as in the Langley Mach-10 tunnel, but a detailed picture was not obtained due to the limited number of measurements made. Waves measured in the Langley Mach 10 tunnel and Tunnel 9 could be compared to each other and to computations at one condition. The comparison suggests that freestream noise may be creating larger waves in the Langley Mach-10 tunnel than in Tunnel 9.

In addition, it was shown that records on the order of 1 ms are sufficient for wave detection in Tunnel 9. Waves could also be detected in Tunnel 9 with record lengths as short as a single FFT encompassing 8–10 wave cycles, though the intermittency of the waves and noise in the FFT make detection difficult. In Tunnel 9, measurements of transition using thermocouples, Kulites, and PCBs were compared. What appears to be a long transition region was found at $Re/m = 13.5 \times 10^6$ with both the Kulites and the thermocouples. Additional comparisons of the same type in the Langley tunnels were not possible due to the lack of thermocouples and the lack of transitional peaks in the Kulite data.

American Institute of Aeronautics and Astronautics

VIII.   Future Work

This is not a complete analysis of the data set that was obtained in the tests in these wind tunnels. The data in these tunnels should be compared to the data already acquired at Purdue and Sandia.[7] More computations should be performed to compare predicted second-mode wave frequencies and growth with the measurements. Such computations can also be used to compare N factors to the appearance of harmonics, wave saturation, and breakdown. The data obtained using blunt nosetips, roughness elements and angle of attack will be examined in the future and compared to the present results. In addition, the Pitot-probe measurements in Tunnel 9 and NASA Langley should be compared to each other as well as to the PCB measurements made on the cone.

More measurements in Tunnel 9 are needed in order to observe wave breakdown. In particular, Tunnel 9 is capable of performing a Reynolds number sweep during a single run. Such runs should be performed for future measurements. Additional measurements in the Langley tunnels to observe breakdown at different sensor positions would also be useful. In addition, measurements of transition location using thermocouples and Kulites in Langley are needed. In the future, newly manufactured inserts for the cone will allow PCB132 sensors to be installed at more streamwise positions. This will allow more PCBs and Kulites to be placed sequentially, avoiding the gaps that prevented observation of peaks in the transitional pressure fluctuations.

IX.   Acknowledgements

References

[1]Mack, L. M., "Boundary-Layer Linear Stability Theory," *Special Course on Stability and Transition of Laminar Flow*, AGARD-R-709, chap. 3, June 1984, pp. 3–1:3–81.

[2]Stetson, K., Kimmel, R., Thompson, E., Donaldson, J., and Siler, L., "A Comparison of Planar and Conical Boundary Layer Stability at a Mach Number of 8," Paper 91-1639, AIAA, June 1991.

[3]Stetson, K. F. and Kimmel, R. L., "Example of Second-Mode Instability Dominance at a Mach Number of 5.2," *AIAA Journal*, Vol. 30, No. 12, December 1992, pp. 2974–2976.

[4]Schneider, S. P., "Hypersonic Laminar-Turbulent Transition on Circular Cones and Scramjet Forebodies," *Progress in Aerospace Sciences*, Vol. 40, 2004, pp. 1–50.

[5]Fujii, K., "Experiment of Two Dimensional Roughness Effect on Hypersonic Boundary-Layer Transition," *Journal of Spacecraft and Rockets*, Vol. 43, No. 4, July-August 2006, pp. 731–738.

[6]Estorf, M., Radespiel, R., Schneider, S. P., Johnson, H., and Hein, S., "Surface-Pressure Measurements of Second-Mode Instability in Quiet Hypersonic Flow," Paper 2008-1153, AIAA, January 2008.

[7]Casper, K. M., Beresh, S. J., Henfling, J. F., Spillers, R. W., Pruett, B., and Schneider, S. P., "Hypersonic Wind-Tunnel Measurements of Boundary-Layer Pressure Fluctuations," Paper 2009-4054, AIAA, June 2009, revised November 2009.

[8]Tanno, H., Komuro, T., Sato, K., Itoh, K., Takahashi, M., and Fujii, K., "Measurement of Hypersonic Boundary Layer Transition on Cone Models in the Free-Piston Shock Tunnel HIEST," Paper 2009-0781, AIAA, January 2009.

[9]Roediger, Knauss, Kraemer, Heitmann, D., Radespiel, Smorodsky, Bountin, D., and Maslov, A., "Hypersonic Instability Waves Measured on a Flat Plate at Mach 6," *International Conference on Methods of Aerophysical Research*, July 2008.

[10]Beckwith, I. E. and Miller III, C. G., "Aerothermodynamics and Transition in High-Speed Wind Tunnels at NASA Langley," *Annual Review of Fluid Mechanics*, Vol. 22, 1991, pp. 419–439.

[11]Schneider, S. P., "Flight Data for Boundary-Layer Transition at Hypersonic and Supersonic Speeds," *Journal of Spacecraft and Rockets*, Vol. 36, No. 1, 1999, pp. 8–20.

[12]Chen, F.-J., Malik, M., and Beckwith, I., "Boundary-Layer Transition on a Cone and Flat Plate at Mach 3.5," *AIAA Journal*, Vol. 27(6), June 1989, pp. 687–693.

[13]Ward, C., Wheaton, B. M., Chou, A., Gilbert, P. L., Steen, L. E., and Schneider, S. P., "Hypersonic Boundary-Layer Transition Experiments in a Mach-6 Quiet Tunnel," Paper 2010-4721, AIAA, June 2010.

[14]Alba, C., Johnson, H., Bartkowicz, M., Candler, G., and Berger, K., "Boundary Layer Stability Calculations for the HIFiRE-1 Transition Experiment," *Journal of Spacecraft and Rockets*, Vol. 45, No. 6, January 2008, pp. 1125–1133.

[15]Pate, S. R., "Measurements and Correlations of Transition Reynolds Numbers on Sharp Slender Cones at High Speeds," *AIAA Journal*, Vol. 9, No. 6, 1971, pp. 1082–1090.

[16]Ragsdale, W. C. and Boyd, C. F., *Hypervelocity Wind Tunnel 9 Facility Handbook, Third Edition*, Silver Spring, MD, July 1993, NAVSWC TR 91-616.

[17]Micol, J. R., "Langley Aerothermodynamics Facilities Complex: Enhancements and Testing Capabilities," Paper 1998-0147, AIAA, January 1998.

[18]Casper, K. M., *Hypersonic Wind-Tunnel Measurements of Boundary-Layer Pressure Fluctuations*, Master's thesis, Purdue University School of Aeronautics and Astronautics, August 2009.

[19]Beresh, S., Henfling, J., Spillers, R., and Pruett, B., "Measurement of Fluctuating Wall Pressures Beneath a Supersonic Turbulent Boundary Layer," No. 2010-305, January 2010.

[20]Wheaton, B. M., Juliano, T. J., Berridge, D. C., Chou, A., Gilbert, P. L., Casper, K. M., Steen, L. E., Schneider, S. P., and Johnson, H. B., "Instability and Transition Measurements in the Mach-6 Quiet Tunnel," Paper 2009-3559, AIAA, June 2009.

[21]Alba, C., Casper, K., Beresh, S., and Schneider, S., "Comparison of Experimentally Measured and Computed Second-Mode Disturbances in Hypersonic Boundary-Layers," Paper 2010-897, AIAA, January 2010.

[22]Berridge, D., Chou, A., Ward, C., Steen, L., Gilbert, P., Juliano, T., Schneider, S., and Gronvall, J., "Hypersonic Boundary-Layer Transition Experiments in a Mach-6 Quiet Tunnel," Paper 2010-1061, AIAA, January 2010.

[23]Pate, S. R. and Brown, M. D., "Acoustic Measurements in Supersonic Transitional Boundary Layers," Tech. Rep. AEDC-TR-69-182, Arnold Engineering Development Center, October 1969.

[24]Johnson, R. I., Macourek, M. N., and Saunders, H., "Boundary Layer Acoustic Measurements in Transitional and Turbulent Flow at $M_\infty = 4.0$," AIAA Paper 69-344, April 1969.

[25]Cassanto, J. M. and Rogers, D. A., "An Experiment to Determine Nose Tip Transition with Fluctuating Pressure Measurements," *AIAA Journal*, Vol. 13, No. 10, 1975, pp. 1257–1258.

[26]Martellucci, A., Chaump, L., Rogers, D., and Smith, D., "Experimental Determination of the Aeroacoustic Environment about a Slender Cone," *AIAA Journal*, Vol. 11, No. 5, 1973, pp. 635–642.

[27]Pate, S. R., "Dominance of Radiated Aerodynamic Noise on Boundary-Layer Transition in Supersonic/Hypersonic Wind Tunnels," Tech. Rep. AEDC-TR-77-107, Arnold Engineering Development Center, March 1978.

[28]Wright, M. J., Candler, G. V., and Bose, D., "A Data-Parallel Line-Relaxation Method for the Navier-Stokes Equations," Paper 97-2046CP, AIAA, June 1997.

[29]Johnson, H. B. and Candler, G. V., "Hypersonic Boundary Layer Stability Analysis Using PSE-Chem," Paper 2005-5023, AIAA, June 2005.

[30]Glowacki, W. J., "NOL Hypervelocity Wind Tunnel Report No. 2: Nozzle Design," NOLTR 71-6, Naval Ordnance Lab., White Oak, Silver Spring, MD, April 1971.

[31]Berridge, D., *Measurements of Second-Mode Waves in Hypersonic Boundary Layers with a High-Frequency Pressure Transducer*, Master's thesis, Purdue University, 2010, To be published December 2010.

[32]VanDercreek, C., Smith, M., and Yu, K., "Hypersonic Flow Measurements using Focused Schlieren and Deflectometry at AEDC Hypervelocity Wind Tunnel No. 9," Tech. Rep. 2010-4209, AIAA, June 2010.

[33]Pate, S. R. and Schueler, C. J., "Radiated Aerodynamic Noise Effects on Boundary-Layer Transition in Supersonic and Hypersonic Wind Tunnels," *AIAA Journal*, Vol. 7, No. 3, 1969, pp. 450–457.

[34]Pate, S. R., "Effects of Wind-Tunnel Disturbances on Boundary-Layer Transition with Emphasis on Radiated Noise: A Review," AIAA Paper 1980-0431, March 1980.